

Designing Pseudocapacitance for Nb₂O₅/Carbide-Derived Carbon Electrodes and Hybrid Devices

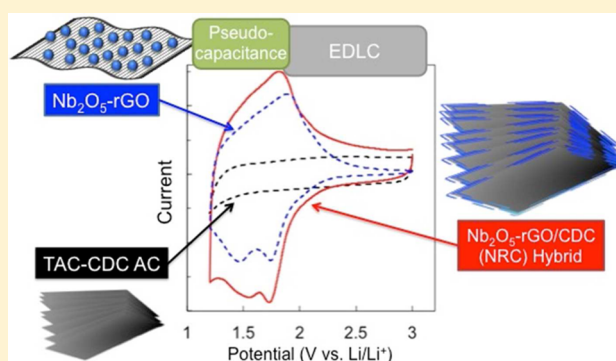
Chun-Han Lai,[†] David Ashby,[†] Melissa Moz,[†] Yury Gogotsi,[‡] Laurent Pilon,[§] and Bruce Dunn^{*,†,||}

[†]Department of Materials Science and Engineering, [§]Department of Mechanical and Aerospace Engineering, and ^{||}The California NanoSystems Institute, University of California, Los Angeles, California 90095, United States

[‡]Department of Materials Science and Engineering and A. J. Drexel Nanomaterials Institute, Drexel University, Philadelphia, Pennsylvania 19104, United States

Supporting Information

ABSTRACT: Composite structures for electrochemical energy storage are prepared on the basis of using the high-rate lithium ion insertion properties of Nb₂O₅. The Nb₂O₅ is anchored on reduced graphene oxide (rGO) by hydrothermal synthesis to improve the charge-transfer properties, and by controlling the surface charge, the resulting Nb₂O₅-rGO particles are attached to a high-surface-area carbide-derived carbon scaffold without blocking its exfoliated layers. The electrochemical results are analyzed using a recently published multiscale physics model that provides significant insights regarding charge storage kinetics. In particular, the composite electrode exhibits surface-confined charge storage at potentials of <1.7 V (vs Li/Li⁺), where faradaic processes dominate, and electrical double layer charge storage at potentials of >2.2 V. A hybrid device composed of the composite electrode with activated carbon as the positive electrode demonstrates increased energy density at power densities comparable to an activated carbon device, provided the hybrid device operates in the faradaic potential range.



1. INTRODUCTION

Energy storage devices have received considerable attention because of the growing demand for powering portable electronics, the electrification of transportation, and providing grid-level energy storage for renewables.^{1–3} Although lithium ion batteries with high energy density are widely used in these applications, electrical double layer capacitors (EDLCs) based on carbon electrodes offer higher power and shorter charging times and are frequently used to complement or even replace batteries provided low energy density is acceptable.^{4–7} To overcome the energy density limitations of EDLCs, a second mechanism for capacitive energy storage, pseudocapacitance, has received considerable interest because charge storage in these materials is based on reversible redox reactions occurring at or near the surface.^{6,8–11} A variety of transition-metal oxides (TMOs) have been identified as pseudocapacitor materials.^{12–16} Charge storage with TMOs such as RuO₂, MnO₂, and Nb₂O₅ reaches much higher levels than the EDLCs and offers the prospect of achieving energy densities of lithium ion battery materials but with the ability to operate at high power.^{17–19}

This article is based on orthorhombic niobium oxide (T-Nb₂O₅) in which rapid insertion/deinsertion of lithium throughout the entire material leads to high energy density. Lithium contents of up to Li/Nb = 1 occur without a phase change. Preferred ion transport along specific crystallographic

pathways in T-Nb₂O₅ is considered to be responsible for achieving the high energy density at high rates.^{20–22} Unfortunately, the poor electronic conductivity of Nb₂O₅ (10⁻⁶ S cm⁻¹) limits its performance in thick electrodes.²¹ For this reason, there has been considerable effort in fabricating composite electrodes composed of nanostructured Nb₂O₅ with different carbons. Among the systems that provide effective electronic conducting pathways are carbon nanotubes (CNT), reduced graphene oxide (rGO), and amorphous carbon coatings.^{23–25} These carbon additives successfully improve charge transfer by forming direct oxide–carbon bonds. Moreover, by growing Nb₂O₅ on carbon, the oxide nanoparticles can be homogeneously dispersed on the carbon and the Nb₂O₅ can be effectively “wired” to provide electronic conduction.^{26–28} The conductive additive need not be carbon. In a recent paper, a niobium carbide, MXene (Nb₂CT_x), was used as a precursor to form a hierarchical structure in which Nb₂O₅ was grown on the parent MXene with disordered carbon.^{29,30} Another important feature for constructing reliable

Special Issue: Fundamental Interfacial Science for Energy Applications

Received: March 31, 2017

Revised: May 19, 2017

Published: May 25, 2017

electrodes is their porosity, which can be manipulated by using different carbon components and corresponding processing.³¹ The pore network enables electrolyte access to the redox-active material.

The studies involving adding conductive additives to Nb₂O₅ have enabled the fabrication of electrodes that have thicknesses in the range of several tens of micrometers. These structures are suitably thick for demonstrating device operation. However, aside from energy density and power density measurements, there has been relatively little insight regarding charge storage mechanisms in these materials. Here, we analyze our experimental results using a recent model reported by Girard et al. that characterized a three-electrode configuration with Nb₂O₅ as the working electrode and LiClO₄ in propylene carbonate as the electrolyte.³² The authors used a continuum approach based on the generalized modified Poisson–Nernst–Planck (GMPNP) model for a binary symmetric electrolyte with faradaic reactions.^{33–36} The simulations qualitatively reproduce the experimentally measured cyclic voltammogram (CV) curves and provide significant insights regarding interfacial and transport phenomena and charge storage. In particular, the simulations show potential regions where currents are dominated by either electrical double layer processes (formed by ClO₄[−]) or redox reactions associated with Li⁺ insertion/deinsertion. An example of the simulated CV during discharge and charge is shown in Figure S1. Another feature we consider in this paper is the transition between the capacitive and faradaic potential regions. As explained later in the article, the peak current in the CV is a function of the sweep rate (ν)^{10,37}

$$I = a\nu^b \quad (1)$$

where the exponent, b , is an indication of whether currents are diffusion-controlled ($b = 0.5$) or surface-controlled ($b = 1$).¹⁰ The simulation shows that $b = 1$ both in the capacitive and faradaic regimes, with a decrease to $b \approx 0.6$ at the potential corresponding to the transition between these regimes. In this article, we apply this analysis to the operation of an asymmetric supercapacitor device.

This article is based on using carbide-derived carbon (CDC) as a porous conductive scaffold for a hybrid material consisting of Nb₂O₅ nanoparticles deposited on rGO (referred to as Nb₂O₅-rGO). This work builds on an earlier study in which the deposition of Nb₂O₅ on CDC was poorly controlled and some 80% of the surface area was lost, blocking electrolyte access to the redox-active Nb₂O₅.³⁸ In the current work, we successfully fabricated composite electrode structures in which Nb₂O₅-rGO and CDC particles were uniformly assembled by delicately controlling their zeta potentials. These particles uniformly cover the surface of CDC layered structures that remain unblocked and facilitate electrolyte access. This approach also avoids Nb₂O₅ particles forming unfavorable oxide–oxide contacts. The resulting Nb₂O₅-rGO particles are responsible for the high energy density at high rate exhibited by the Nb₂O₅-CDC electrode. We then incorporate this material into an asymmetric supercapacitor that operates largely in the pseudocapacitive region identified by the simulation.

2. EXPERIMENTAL SECTION

2.1. Preparation of GO, Nb₂O₅-rGO, and NRC Materials. The material described in this article consists of three components that work together synergistically. Redox-active material Nb₂O₅ is synthesized on sheets of reduced graphene oxide (rGO), which

provides electronic conduction for the charge-transfer reactions. These Nb₂O₅-rGO particles are processed using an ethanol suspension so that they assemble on layers of CDC particles. The resulting materials are termed NRC (the letter for each component) and identified by the weight ratio between Nb₂O₅-rGO and CDC.

Graphene oxide was synthesized by a modification of Hummer's method.³⁹ Details of this process are provided in the Supporting Information. The Nb₂O₅-rGO particles were prepared using a hydrothermal method followed by annealing at 500 °C in Ar. Thermogravimetric analysis (TGA) shows that the Nb₂O₅-rGO particles are 89 wt % Nb₂O₅ (Figure S2). NRC particles were prepared by mixing Nb₂O₅-rGO and CDC (TAC-CDC from Y-carbon) in ethanol. Ethanol suspensions (1 g L^{−1}) of CDC and Nb₂O₅-rGO were prepared separately with good stability by adding 5 mM NH₄OH (Sigma-Aldrich, 28–30% NH₃) using ultrasonication. The as-prepared suspensions have pH values of between 9.9 and 10.2. Zeta potential measurements indicate that the CDC and Nb₂O₅-rGO have opposite surface charges and that the surface charge concentration on both particles was stable after the 5 mM NH₄OH addition (Figure S3). The Nb₂O₅-rGO and CDC suspensions were mixed together in different ratios under vigorous stirring. By having an opposite surface charge to that of CDC, Nb₂O₅-rGO forms a uniform layer on CDC to produce NRC particles. The NRC particles were kept in an oven at 80 °C overnight to remove the solvent, followed by further dehydration at 110 °C in a vacuum oven before being made into electrodes. The NRC particles were denoted by their Nb₂O₅-rGO weight ratios, such as NRC-20 (Nb₂O₅-rGO/CDC = 20:80), NRC-40 (Nb₂O₅-rGO/CDC = 40:60), and NRC-60 (Nb₂O₅-rGO/CDC = 60:40).

2.2. Material Characterization. Zeta potential measurements (Zetasizer, Malvern Instruments) were made on the CDC and Nb₂O₅-rGO solutions used in the NRC preparation. Transmission electron microscopy (TEM; CM 120, FEI) and scanning electron microscopy (SEM; Nova 230 Nano SEM) were used to characterize the surface morphologies for Nb₂O₅-rGO and NRC. Energy-dispersive XRD spectroscopy (EDX) was used to determine the elemental distribution in NRC electrodes. Thermogravimetric analysis (TGA; SDT Q-600, TA Instruments) was used to determine the amount of oxide in Nb₂O₅-rGO as well as the moisture content and overall thermal stability. X-ray diffraction (XRD; PANalytical, X'PertPro) using Cu K α radiation ($\lambda = 1.54 \text{ \AA}$) and Raman spectra (Renishaw inVia) with a 514 nm laser line were used to identify the crystallinity of Nb₂O₅-rGO and the bonding properties of rGO after annealing, respectively. The Brunauer–Emmett–Teller (BET) surface area and pore size distribution analysis were carried out by using a gas adsorption apparatus (Micromeritics ASAP 2010) with N₂ adsorption isotherms at 77 K. Four-point probe measurements with a VMP potentiostat/galvanostat (Bio-Logic) were used to determine the electrical resistivity of NRC electrodes.

2.3. Electrochemical Measurements. The NRC material was prepared as a conventional electrode in which NRC particles were mixed with poly(vinylidene fluoride) (PVdF) in a 9:1 weight ratio in an *N*-methyl-2-pyrrolidone (NMP) solution to form a uniform slurry. The electrodes were sufficiently conductive so that no additional carbon was required. The slurry was spread on a stainless steel foil by using a doctor blade and dried in a vacuum oven at 110 °C. To make electrodes, the sample-loaded foils were punched into 1 cm² discs, leading to a mass loading of 1–1.2 mg cm^{−2} and a thickness of 40 to 70 μm depending on the NRC composition. Two control electrodes, 100% CDC electrodes (CDC/PVdF = 80:20 wt %) and 100% Nb₂O₅-rGO electrodes (Nb₂O₅-rGO/PVdF = 90:10 wt %), were prepared by this route. The electrodes were tested in a two-electrode configuration using a Swagelok cell with a lithium counter electrode and a 1 M LiClO₄ in EC/DMC (1:1 in volume) electrolyte. For full-cell testing, NRC negative electrodes were paired with positive electrodes composed of YPS0F activated carbon (AC), carbon nanotubes (CNTs), and PVdF in a weight ratio of 85:5:10. The multiwalled CNTs (Sigma-Aldrich) had an outer diameter of 10 nm, an inner diameter of 4.5 nm, and a varied length from 3 to 6 μm . The weight ratio between the AC and NRC is kept at 3:1 to compensate for their

capacity difference. In addition to the NRC electrodes, the electrochemical properties of the Nb_2O_5 -rGO electrode material were also investigated. For these experiments, a thin-film electrode was prepared by drop casting a suspension of the Nb_2O_5 -rGO material on a $1 \times 1 \text{ cm}^2$ stainless steel substrate. The thin-film electrodes were tested in a three-electrode flooded cell that contains 1 M LiClO_4 in EC/DMC (1:1 by volume) as the electrolyte and two Li foils serving as counter and reference electrodes. The mass loading for the thin-film electrode, $\sim 30 \mu\text{g}/\text{cm}^2$, was measured by using a microbalance with 0.1 μg resolution. This electrode contained neither a binder nor a conductive additive.

Cyclic voltammetry (CV) and galvanostatic charge–discharge (GCD) measurements were made using a VMP potentiostat/galvanostat (Bio-Logic) at 1.2–3 V versus Li/Li^+ for half-cell and 1–2.8 V for full-cell devices. The specific capacity C (C g^{-1}) was determined for different NRC electrodes from their CV curves from the following equation

$$C = \int_{V_1}^{V_2} \frac{I \, dV}{mv}$$

where I is the measured current response (mA), m is the mass loading of the active materials, V_1 and V_2 are the initial and final potentials (V), and v is the sweep rate (mV s^{-1}). For half cells, the mass used in the calculation was the weight of the NRC electrode, but without binder (these electrodes did not contain any additional conductive additive). For full cells, the mass used was the weight of the NRC electrode (without binder) plus the weight of the YP50F component. For the GCD measurements, electrodes were cycled at different C rates using $1 \text{ C} = 30 \text{ mA g}^{-1}$.

3. RESULTS AND DISCUSSION

3.1. Characterization of Nb_2O_5 -rGO. Figure 1 shows as-prepared Nb_2O_5 -rGO after annealing. TEM images in Figure 1a

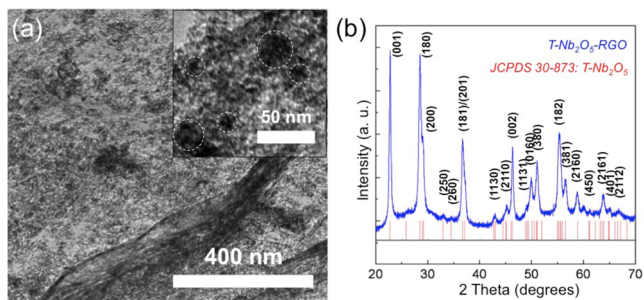


Figure 1. Morphology and structure of Nb_2O_5 -rGO particles after annealing. (a) TEM image for Nb_2O_5 -rGO. Particles of Nb_2O_5 are outlined in the inset. (b) XRD pattern for postannealed Nb_2O_5 -rGO sheets compared to the JCPDS data for orthorhombic Nb_2O_5 .

show that the Nb_2O_5 nanoparticles were uniformly grown on the rGO sheet, which retains its flexible nature with folding and wrinkles. The inset shows the contrast between particles (darker) and the sheet underneath, indicating that their size ranges from 15 to 25 nm. Figure 1b shows that the XRD pattern for the annealed Nb_2O_5 -rGO matches that of the orthorhombic T phase by JCPDS 30-873. The average crystallite size derived from Scherrer's equation is $15 \pm 4 \text{ nm}$,⁴⁰ which is consistent with the particle sizes observed in Figure 1a. As indicated previously, the carbon content of the annealed Nb_2O_5 -rGO was also confirmed to be 11 wt % by using TGA analysis (Figure S2).

3.2. Characterization of NRC Particles and Their Electrodes. The opposite surface charges for Nb_2O_5 -rGO and CDC are instrumental in fabricating an electrode architecture in which a redox-active phase is embedded in the

carbon matrix and yet its electrochemical properties are prominent. SEM images for NRC particles prepared at different mixing ratios are shown in Figure 2. Figure 2a shows pristine

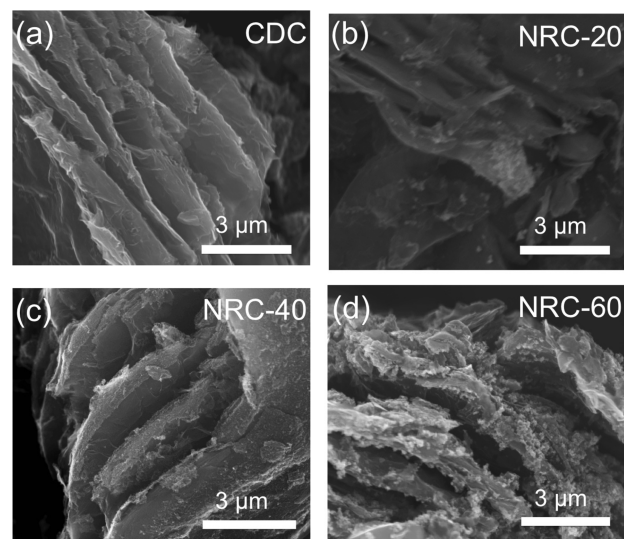


Figure 2. SEM images for (a) CDC, (b) NRC-20, (c) NRC-40, and (d) NRC-60. The exfoliated layers of CDC are retained in all NRC samples, although NRC-60 shows evidence of particle stacking as opposed to isolated particles.

CDC, which exhibits exfoliated layers with micrometer-scale spacing created by the chlorination process at $800 \text{ }^\circ\text{C}$.⁵ Figure 2b–d shows the NRC particles for compositions ranging from 20 to 60 wt % Nb_2O_5 -rGO. For the NRC-20 (Figure 2b), the Nb_2O_5 -rGO sheets cover relatively few outside layers of CDC. In Figure 2c, NRC-40 shows preferential Nb_2O_5 -rGO coverage on the CDC edges. More importantly, this image and that of Figure 2d show that the Nb_2O_5 -rGO particles do not clog the CDC microstructures and that the open-layered structure of the CDC is retained, even for NRC-60 where the additional Nb_2O_5 -rGO particles cover nearly all of the CDC layers. On the basis of these results, it would seem that controlling the surface charge prevents particle aggregation that would obstruct electrolyte access to the NRC electrode. The pore size distribution (Figure S4) determined by using the BJH analysis of adsorption isotherms is consistent with the images in Figure 2 because this distribution is virtually unchanged by the attachment of Nb_2O_5 -rGO to CDC. The most probable pore diameter of the CDC, 3.8 nm, is retained in the NRC-40 material, as is the broad distribution of mesopores extending to 50 nm. In contrast, Nb_2O_5 -rGO exhibits no measurable porosity. On the basis of these results, it is not surprising that the surface area scales almost linearly with the CDC content, ranging from $828 \text{ m}^2 \text{ g}^{-1}$ for pure CDC to $374 \text{ m}^2 \text{ g}^{-1}$ for NRC-60 (Figure S4 and Table 1). It is important to note that the NRC particles exhibit a high surface area, with NRC-40 having a surface area of nearly $600 \text{ m}^2/\text{g}$. The retention of high surface area ensures that the double-layer capacitance of the CDC will contribute to the charge storage of the NRC material.

Table 1 also lists the effective electrical resistivity and calculated porosity for different NRC electrodes along with the control sample electrodes, CDC and Nb_2O_5 -rGO. The NRC electrodes contain no additional carbon beyond that coming from the CDC and rGO used in the synthesis. EDX elemental mapping shows that the Nb_2O_5 -rGO and CDC components are

Table 1. Physical Properties for Different NRC Samples and Their Components, Nb₂O₅-rGO and CDC

electrode formula (active materials/PVdF)	BET surface area of active materials (m ² g ⁻¹)	electrode resistivity (Ω cm)	bulk density (g cm ⁻³)	calculated porosity (%)
CDC (80/20)	828 ± 40	0.15	0.17	91.8 ± 0.4
NRC-20 (90/10)	660 ± 41	0.23	0.23	91.1 ± 0.2
NRC-40 (90/10)	585 ± 54	0.28	0.25	91.4 ± 0.5
NRC-60 (90/10)	374 ± 60	0.38	0.25	92.4 ± 0.6
Nb ₂ O ₅ -rGO (90/10)	66 ± 34	0.77	0.38	75.8 ± 1.5

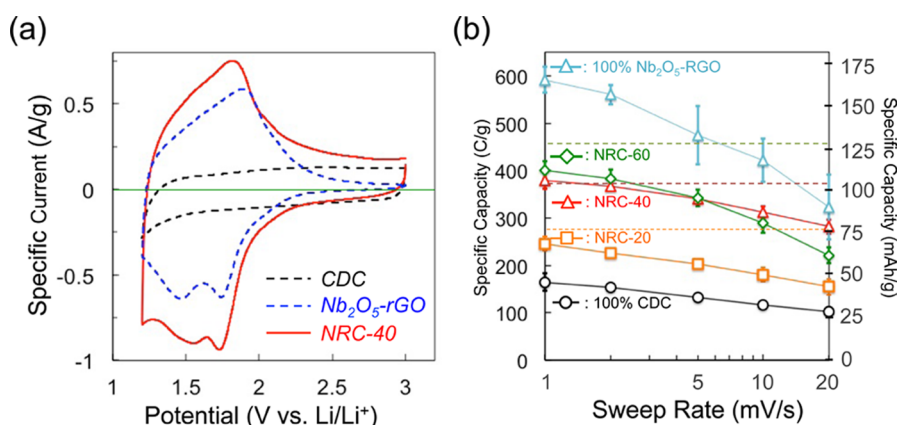


Figure 3. Energy storage properties for NRC samples and the components, Nb₂O₅-rGO and CDC. (a) Characteristic CV curves at a sweep rate of 2 mV s⁻¹. (b) Sweep rate dependence of the specific capacitance as derived from the CV curves. The specific capacity values are normalized to the weight of the NRC electrode, excluding the weight of the binder. The dashed lines represent the capacities calculated from the weight ratios for the Nb₂O₅-rGO and CDC components and their specific capacity values at 1 mV s⁻¹ (Nb₂O₅-rGO, 180 mAh g⁻¹; CDC, 50 mAh g⁻¹).

distributed uniformly in the NRC electrode (Figure S5-a). The NRC resistivity decreases continuously with increasing CDC content. This indicates that CDC provides an effective pathway for electronic conduction in the NRC electrodes. Compared to CDC, the rGO sheets are less conductive, probably because of the structural defects identified by Raman spectroscopy (Figure S5-b). Thus, the pure Nb₂O₅-rGO particles exhibit the highest resistivity of 0.77 Ω cm. In contrast to the electrical properties, the porosity of NRC electrodes is unaffected by the CDC content, with values slightly greater than 90% for all compositions. This high level of porosity is important because it can provide the electrode with sufficient ion transport through the electrolyte to prevent kinetic losses due to mass transport limitations.¹¹ Overall, the surface area and resistivity values indicate that the synthesis approach for NRC electrodes successfully preserves the microstructures and physical features from individual CDC and Nb₂O₅-rGO constituents.

3.3. Electrochemical Screening of NRC Electrodes.

Figure 3a shows CV signatures at 2 mV s⁻¹ for Nb₂O₅-rGO, CDC, and NRC-40 electrodes. Between 1.2 and 3 V, CDC (black) exhibits the characteristic box shape of an EDLC, whereas Nb₂O₅ (blue) displays a significant increase in current response as it is swept cathodically below 2.0 V, arising from redox reactions. The NRC-40 curve (red) combines CV features from both CDC and Nb₂O₅. Because of its lower resistivity, the voltage offset between the oxidation and reduction redox peaks is less than that of Nb₂O₅-rGO. As indicated by the model developed by Girard et al.,³² the current contribution below 2 V is dominated by the pseudocapacitance from Nb₂O₅, whereas above 2.2 V the contribution from the electrical double layer prevails. The sweep rate dependence of charge storage for the different electrodes (Figure 3b) shows that the capacity of the NRC electrode increases with the

Nb₂O₅-rGO content. In comparing the different NRC compositions, NRC-60 exhibits the highest specific capacity at low sweep rates. Its capacity, however, decreases continuously so that at rates >5 mV s⁻¹ the NRC-40 composition exhibits greater capacity values and retains nearly 300 C g⁻¹ at 20 mV s⁻¹. We attribute the poor rate capability in NRC-60 to the stacking of Nb₂O₅-rGO layers as shown in Figure 2d. Not only will this increase the electrode resistivity by forming insulating oxide–oxide interfaces, but it is also likely that some of the Nb₂O₅ will not be exposed to the electrolyte and thus will be unable to contribute to the redox reactions. For these reasons, the NRC-40 electrode was chosen for further electrochemical testing. As a convenient comparison, the capacities calculated by the rule of mixtures for the Nb₂O₅-rGO and CDC components are indicated by the dashed line in Figure 3b. The better kinetics of NRC-40 are indicated by exhibiting less deviation in capacity compared to that of NRC-60.

3.4. Pseudocapacitance in the Nb₂O₅-rGO Thin Electrode.

Cyclic voltammetry offers a convenient measurement approach for distinguishing between the different energy storage properties that characterize EDLCs and battery materials.⁸ Equation 1 provides a basis for this distinction because battery materials are characterized by faradaic reactions limited by semi-infinite diffusion ($b = 0.5$). In contrast, capacitive storage is characterized by currents that are linear with the scan rate ($b = 1$). The $b = 1$ values also describe the currents due to surface-confined redox processes that represent a pseudocapacitance.⁸ That is, pseudocapacitive materials resemble a battery material in that a redox reaction is involved in charge storage, but it is also different because the kinetics are not diffusion controlled by bulk processes. In this article, we use b values derived from the simulations of Girard et al. to provide

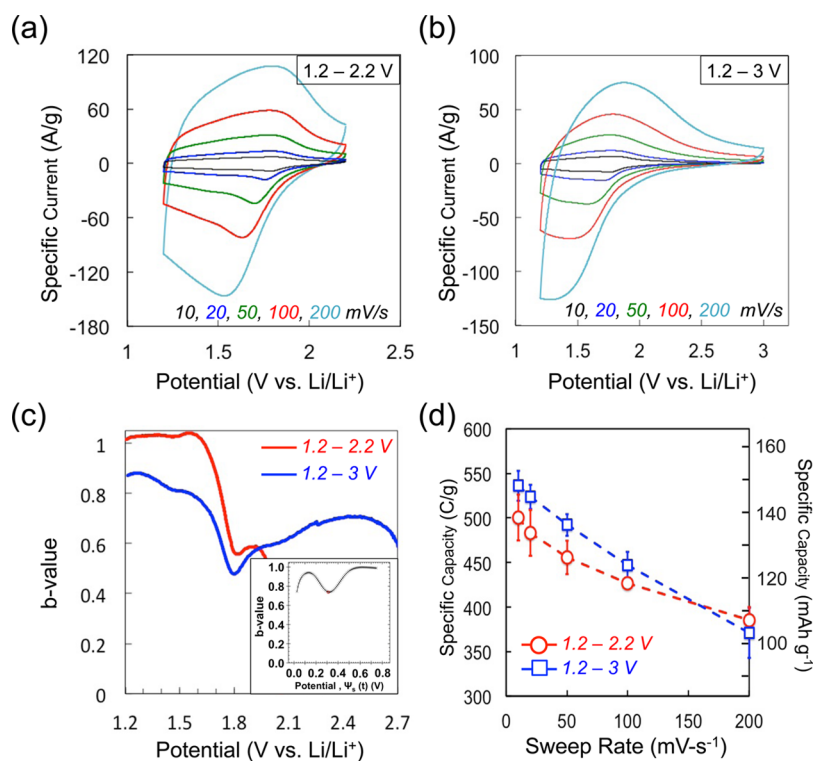


Figure 4. Cyclic voltammetry experiments and analysis for Nb_2O_5 -rGO thin-film electrodes. (a) Sweep rate dependence between 1.2 and 2.2 V (vs Li/Li^+). Over this potential range, Nb_2O_5 is lithiated and charge storage occurs through redox reactions. (b) Sweep rate dependence between 1.2 and 3.0 V (vs Li/Li^+). In this potential range, charge storage is from both double-layer capacitance and redox reactions. The dip at ~ 1.8 V is associated with the transition between the faradaic and capacitive potential regions. (c) Variation in the b value as a function of potential for the two different potential regimes. The dip at ~ 1.8 V is associated with the transition between the faradaic and capacitive potential regions. The inset shows the b -value variation for Nb_2O_5 derived from a simulation.³² (d) Sweep rate dependence of the specific capacity for Nb_2O_5 -rGO samples that operate over different potential ranges.

insight regarding charge storage in Nb_2O_5 -rGO and NRC electrode materials.

Cyclic voltammetry experiments on Nb_2O_5 -rGO electrode materials were carried out using different potential ranges as shown in Figure 4a,b. These experiments used thin film electrodes in order to provide better comparisons with the simulations. The samples cycled in the range between 1.2 and 2.2 V (vs. Li/Li^+) are designed to remain partially lithiated during the entire cycle, whereas the Nb_2O_5 -rGO electrodes cycled up to 3 V are expected to be fully delithiated at the end of oxidation. According to the simulations of Girard et al., the former electrodes function in the potential region where only faradaic reactions occur whereas the delithiated sample operates in both the capacitive and faradaic regions. By using the CV curves in Figure 4a,b, we derived b -value variations with potential for partially lithiated (red) and fully delithiated (blue) Nb_2O_5 -rGO during the lithiation/delithiation process (Figure 4c). The inset in Figure 4c shows the b values reported by Girard et al. for comparison. The red curve exhibits a b value of close to 1 between 1.2 and 1.7 V before decreasing to ~ 0.6 at 1.8 V. This potential is consistent with the response reported by Girard et al., who attributed the dip to interfacial and transport properties associated with the transition between capacitive and faradaic charge-storage processes. These results show that retaining lithium in the Nb_2O_5 -rGO electrode enables redox reactions whose kinetics ($b = 1$) are not diffusion-limited. Another important consideration here is that the presence of lithium in the structure will increase the electronic conductivity.²¹

The Nb_2O_5 -rGO electrode (blue) that undergoes delithiation on oxidation shows no evidence of $b = 1$ despite its operation in the potential range (>2.4 V) where double-layer capacitance should dominate charge storage and at low potentials (<1.7 V) where faradaic reactions occur. Instead, the b values are on the order of 0.7 at potentials above 2.2 V and vary between 0.7 and 0.9 in the lower potential ranges. The analysis by Girard et al. suggests that mass transport limitations of Li^+ may occur near the transition between the capacitive and faradaic regimes. Thus, we might expect that when there are mass transport contributions associated with the measured current, we can expect the b values to be less than 1.0 and as low as 0.5.

The sweep rate dependence for charge storage (Figure 4d) indicates that the specific capacitance decreases with increasing sweep rate for both electrodes. The interesting feature here is that the voltage ranges are quite different (total voltage: 1.0 vs 1.8 V) and yet the amount of stored charge is comparable. Moreover, the specific capacitance for the sample operating in the faradaic range (1.2 to 2.0 V) is actually greater than that for the electrode operating over the wider potential range. Thus, for the Nb_2O_5 -rGO electrode there is no energy storage penalty upon limiting the potential to just the faradaic regime. This is an important consideration for device operation.

3.5. Kinetics of the NRC-40 and NRC-60 Electrodes.

The b -value analysis used for the Nb_2O_5 -rGO electrode was extended to the NRC-40 and NRC-60 electrodes. The mass loading here as well as that of the control samples of CDC and Nb_2O_5 -rGO was 1.0 to 1.2 mg/cm^2 so that these electrodes provide an indication of their performance in relevant devices.

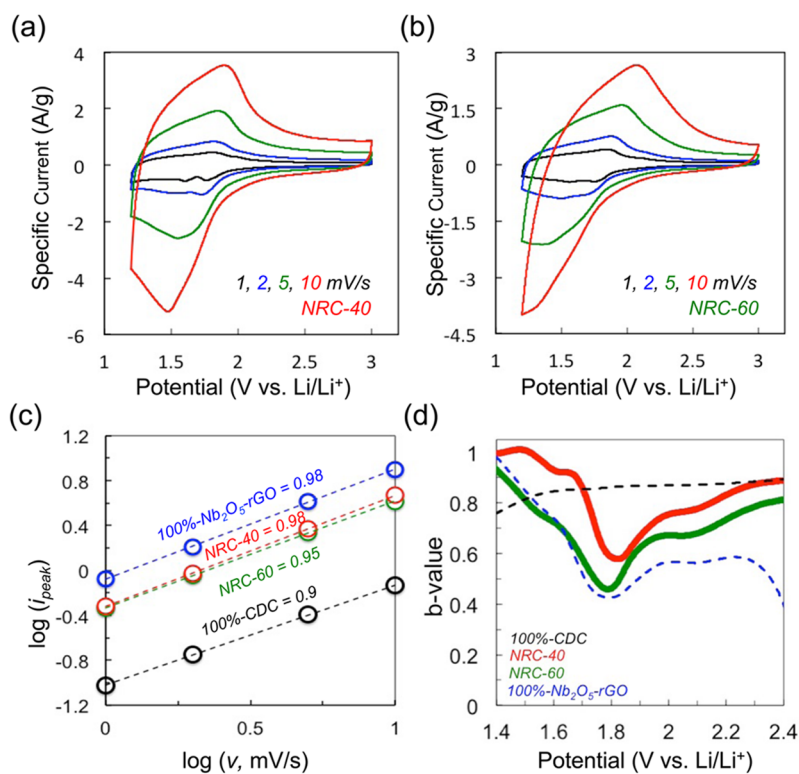


Figure 5. Cyclic voltammetry experiments and analysis for NRC samples and their components, Nb_2O_5 -rGO and CDC. CV curves of between 1 and 10 mV s^{-1} for (a) NRC-40 and (b) NRC-60 electrodes. (c) log–log plot showing the peak current (from CV curves) as a function of sweep rate for NRC samples along with CDC and Nb_2O_5 -rGO. The value of b , which ranges from 0.9 to 1.0, suggests that the charge storage kinetics are surface-controlled. (d) Variation in b value as a function of potential for NRC-40 and NRC-60. The results are compared to the CDC and Nb_2O_5 -rGO components.

The CV curves from 1.2 to 3.0 V (vs Li/Li^+) for NRC-40 and NRC-60 are shown in Figure 5a,b. It is interesting that subtle changes in CV shape and especially that of the redox peaks were also observed in the Girard simulation. The origin of this effect is the increasingly resistive behavior associated with the thicker electrodes.

Equation 1 indicates that the b value is derived from a log–log plot of the peak current, I_{peak} , as a function of sweep rate. Figure 5c shows this analysis for the NRC electrodes and for the control samples of CDC and Nb_2O_5 -rGO. With the exception of the CDC electrode, $b \approx 1$ for all of the electrodes, suggesting that the charge storage kinetics involving Nb_2O_5 on these electrodes are due to a surface-controlled process. For the CDC electrode (obtained at 2 V vs Li/Li^+), the b value is 0.9, in contrast to $b = 1$ that is expected for an electrical double layer capacitor. The possibility here is that the response can be influenced by irreversible charge transfer with residual surface groups associated with the CDC synthesis.^{41,42}

The variation in b value as a function of potential for the NRC electrodes (Figure 5d) seems to exhibit characteristics that combine those of the CDC and the Nb_2O_5 -rGO control electrodes. The dip in b value to 0.5–0.6 at 1.8 V is again an indication of the transition between the faradaic and double-layer capacitance regimes. The b values for both NRC electrodes increase toward 1 at lower potential and toward 0.9 at higher potential as the electrodes approximate the characteristics representative of faradaic and double-layer behaviors, respectively. The change in b value with potential for NRC-40 is more abrupt than that for NRC-60. The b values for both NRC electrodes at the higher potential are much

greater than that of Nb_2O_5 -rGO. This higher b value is an indication that the CDC part of the NRC is contributing to rapid charge storage in this potential range, much more so than Nb_2O_5 -rGO that exhibits $b = 0.5$. Impedance spectra and another analysis that separates the diffusion-controlled and capacitive currents for the NRC electrodes are described in the Supporting Information (Figures S7 and S8). These results are consistent with those of the b values in that significantly more capacitive current (from both faradaic and double-layer contributions) is associated with NRC-40.

The galvanostatic charge–discharge (GCD) behavior provides an indication of how the energy storage of NRC is enhanced through the addition of Nb_2O_5 -rGO particles. In Figure 6, the dependence of specific capacity on potential exhibits two linear regimes. As discussed above, the specific capacity corresponding to the potential range between 3.0 and 1.8 V can be ascribed to the CDC because this is the potential regime where charge storage is generally attributed to the electrical double layer (Figure 5d). The lower slope occurring between 1.8 and 1.2 V is associated with charge storage from redox reactions. This approximation indicates that the specific capacity for a given rate between 0.1 and 4.0 A/g is $\sim 20\%$ from electrical double layer processes and 80% from redox reactions; this ratio seems to change relatively little as a function of rate. The initial results for long-term cycling (Figure S9) indicate that the capacity at high rates (40C) decreases somewhat over 3000 cycles whereas the Coulombic efficiency is nearly 100%.

3.6. NRC//YP50F Capacitors. A hybrid device was fabricated by pairing the NRC-40 electrode with an activated carbon (AC) electrode, YP50F. The CVs for the individual

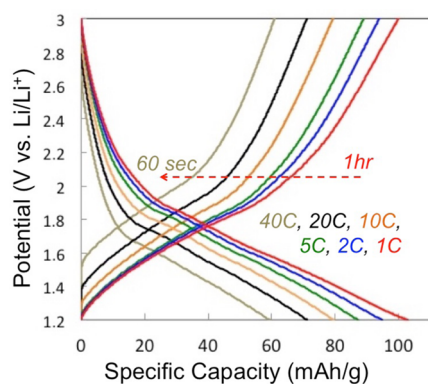


Figure 6. Galvanostatic charge–discharge profiles for a NRC-40 half cell (Swagelok) using a lithium counter electrode. The electrolyte was 1 M LiClO₄ in EC/DMC (1:1 by volume).

NRC-40 and YP50F electrodes after adjusting the weight ratio to 1:3 (to account for the difference in specific capacity) are shown in Figure 7a. Although a fully charged NRC-40//YP50F cell can ideally achieve a potential of 3.2 V, CV plots for the NRC-40//YP50F full cell (Figure 7b) indicate that the potential window for the full cell was optimized between 1 and 2.8 V. The current response over this voltage range is completely capacitive without any irreversible polarization.

Figure 7c shows the charge–discharge profiles for the NRC-40//AC (YP50F) full-cell devices. The GCD curves exhibit the desired linear voltage response from 2 to 200 C. At a rate of 200 C, significant polarization appears with an overall 0.8 V drop in the cell voltage. This sudden potential drop is not caused by the internal series resistance but instead seems to arise from limitations in the NRC electrode performance. Nonetheless, the full cell exhibits reasonable levels of energy

storage at high power, achieving 16 W h kg⁻¹ at 4800 W kg⁻¹. A Ragone plot for the NRC-40//AC full cell is compared to a symmetric activated carbon cell that uses YP50F (Figure 6d). The NRC-40 device shows comparable power density but significantly higher energy density than the AC//AC devices as a result of the pseudocapacitive energy storage in Nb₂O₅.

Additional comparisons between NRC-40//AC and other devices using Nb₂O₅ and AC are detailed in Table 2. These results indicate that the energy density of a device is highly dependent on the Nb₂O₅ content in its electrodes. Because NRC-40//AC contains only 8 wt % Nb₂O₅, it exhibits the lowest energy density of 30 W h kg⁻¹. However, what is most important for hybrid devices is their ability to exhibit high energy density at power levels comparable to those of carbon-based supercapacitors. In Table 2, we compare the different Nb₂O₅-based systems at 3000 W kg⁻¹ and note that the energy density of the NRC hybrid device exceeds that of most other devices that contain much greater amounts of Nb₂O₅. This improved performance is due to both an effective advance in material design and an understanding of the redox properties of the NRC electrode and the potential range where capacitive responses occur. The comparisons in Table 2 show that our design is suitable for high-power applications with an additional economic advantage of using the least amount of Nb₂O₅.

4. CONCLUSIONS

This work reports on the electrochemical energy storage properties of a composite electrode structure that integrates an rGO-anchored redox-active material, Nb₂O₅, which is attached to a high-conductivity, high-porosity CDC scaffold. The Nb₂O₅-rGO particles and CDC scaffold have opposite surface charges, and upon mixing the two components, Nb₂O₅-rGO preferentially attaches onto the edges of the CDC without

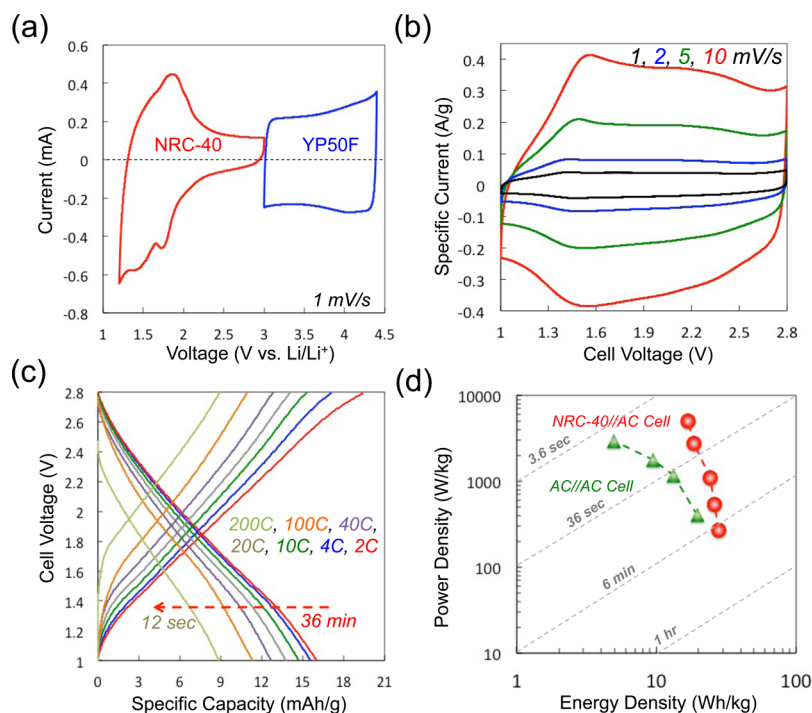


Figure 7. (a) Half-cell CV curves for NRC-40 and activated carbon (AC: YP50F) at a sweep rate of 1 mV s⁻¹. (b) CV curves of NRC-40//AC full cell at different sweep rates. (c) Galvanostatic charge–discharge curves for NRC-40//AC full cell. (d) Ragone plot comparing the AC//AC symmetric cell (0.4–2.8 V) with the NRC//AC hybrid cell (1–2.8 V).

Table 2. Comparison of Hybrid Devices Based on Using Nb₂O₅ as the Negative Electrode and Activated Carbon (AC) as the Positive Electrode

Nb ₂ O ₅ -based negative electrode	AC positive electrode	cell voltage (V)	energy density (W h kg ⁻¹)	energy density at 3000 W kg ⁻¹ (W h kg ⁻¹)	Nb ₂ O ₅ in electrodes (wt %)
Nb ₂ O ₅ nanoparticle ¹⁹	YP17	1–3	40	16	14
mesoporous Nb ₂ O ₅ /carbon ²⁵	MSP-20	1–3	48	29	20
Nb ₂ O ₅ -rGO ²⁶	nonspecified	1–3	56	40	15
Nb ₂ O ₅ -rGO paper ²⁴	mesoporous AC	0.8–3	44	35	16
Nb ₂ O ₅ NP/CNT mixture ²³	nonspecified	0.5–3	34	12	16
Nb ₂ O ₅ @carbon core-shell ²⁸	MSP-20	1–3.5	63	19	16
NRC-40 (this work)	YPS0F	1–2.8	30	23	8

obstructing its layered morphology. The resulting NRC particles retain the high porosity and high electrical conductivity of the pristine CDC and enable electrolyte access to the redox-active material. The NRC is sufficiently conductive that no additional carbon is required to prepare the electrodes. The electrochemical results are analyzed using the model developed recently by Girard et al., which shows potential regions where currents are dominated by either electrical double layer processes or by redox reactions. NRC electrode structures are well explained by this model as *b* values approaching 1 are observed at potentials <1.7 V when faradaic processes dominate charge storage and at potentials >2.2 V when electrical double layers control charge storage. The NRC electrodes were also studied as a 2.8 V hybrid capacitor by pairing with electrodes prepared from activated carbon (YPS0F). By using only 8 wt % Nb₂O₅, the NRC-40//AC hybrid device exhibits reasonable levels of energy storage at power levels comparable to those of carbon-based supercapacitors. The hybrid device achieves 16 W h kg⁻¹ at nearly 5000 W kg⁻¹, properties that exceed those of systems containing much greater amounts of Nb₂O₅. The results for the NRC composite electrodes show the benefits of understanding the importance of both material design and being able to operate in a potential range where pseudocapacitive responses occur.

■ ASSOCIATED CONTENT

📄 Supporting Information

The Supporting Information is available free of charge on the ACS Publications website at DOI: 10.1021/acs.langmuir.7b01110.

Simulated CV curves for Nb₂O₅ based on the GMPNP model, synthesis details for GO and Nb₂O₅-rGO, zeta potential study for NRC preparation, surface area/pore size distribution for NRC particles, EDX elemental mapping for an NRC electrode, Raman spectra for Nb₂O₅-rGO, experimental CV curves for 100% CDC and 100% Nb₂O₅-rGO thick electrodes, kinetic study (*k*₁–*k*₂ analysis) of the diffusion-controlled capacitive current for NRC electrodes, impedance spectra for NRC and Nb₂O₅-rGO electrodes, and cycling behavior of a NRC-40 half cell (PDF)

■ AUTHOR INFORMATION

Corresponding Author

*E-mail: bdunn@ucla.edu.

ORCID

Bruce Dunn: 0000-0001-5669-4740

Notes

The authors declare no competing financial interest.

■ ACKNOWLEDGMENTS

We are grateful for the support of this research from the U.S. Department of Energy, Office of Electricity Delivery and Energy Reliability, Energy Storage System Program through Sandia National Laboratories. Additional support was provided by the Office of Naval Research. The support of the facility for zeta potential measurements from Prof. Tatiana Segura, University of California, Los Angeles, is greatly appreciated.

■ REFERENCES

- (1) Vazquez, S.; Lukic, S. M.; Galvan, E.; Franquelo, L. G.; Carrasco, J. M. Energy storage systems for transport and grid applications. *IEEE Trans. Ind. Electron.* **2010**, *57* (12), 3881–3895.
- (2) Ghadbeigi, L.; Harada, J. K.; Lettiere, B. R.; Sparks, T. D. Performance and resource considerations of Li-ion battery electrode materials. *Energy Environ. Sci.* **2015**, *8* (6), 1640–1650.
- (3) Yang, Z.; Zhang, J.; Kintner-Meyer, M. C.; Lu, X.; Choi, D.; Lemmon, J. P.; Liu, J. Electrochemical energy storage for green grid. *Chem. Rev.* **2011**, *111* (5), 3577–3613.
- (4) Salanne, M.; Rotenberg, B.; Naoi, K.; Kaneko, K.; Taberna, P. L.; Grey, C. P.; Dunn, B.; Simon, P. Efficient storage mechanisms for building better supercapacitors. *Nat. Energy* **2016**, *1*, 16070.
- (5) Beaudin, M.; Zareipour, H.; Schellenberglabe, A.; Rosehart, W. Energy storage for mitigating the variability of renewable electricity sources: An updated review. *Energy Sustainable Dev.* **2010**, *14* (4), 302–314.
- (6) Augustyn, V.; Simon, P.; Dunn, B. Pseudocapacitive oxide materials for high-rate electrochemical energy storage. *Energy Environ. Sci.* **2014**, *7* (5), 1597–1614.
- (7) Aricò, A. S.; Bruce, P.; Scrosati, B.; Tarascon, J. M.; Van Schalkwijk, W. Nanostructured materials for advanced energy conversion and storage devices. *Nat. Mater.* **2005**, *4* (5), 366–377.
- (8) Dylla, A. G.; Henkelman, G.; Stevenson, K. J. Lithium insertion in nanostructured architectures. *Acc. Chem. Res.* **2013**, *46* (5), 1104–1112.
- (9) Chen, C.; Wen, Y.; Hu, X.; Ji, X.; Yan, M.; Mai, L.; Hu, P.; Shan, B.; Huang, Y. Na⁺ intercalation pseudocapacitance in graphene-coupled titanium oxide enabling ultra-fast sodium storage and long-term cycling. *Nat. Commun.* **2015**, *6*, 6929.
- (10) Ardizzzone, S.; Fregonara, G.; Trasatti, S. Inner and “outer” active surface of RuO₂ electrodes. *Electrochim. Acta* **1990**, *35* (1), 263–267.
- (11) Conway, B. E. *Electrochemical Supercapacitors*; Kluwer Academic/Plenum: New York, 1999.
- (12) Kim, H. S.; Cook, J. B.; Tolbert, S. H.; Dunn, B. The development of pseudocapacitive properties in nanosized-MoO₂. *J. Electrochem. Soc.* **2015**, *162* (5), A5083–A5090.
- (13) Yang, P.; Mai, W. Flexible solid-state electrochemical supercapacitors. *Nano Energy* **2014**, *8*, 274–290.

- (14) Lang, X.; Hirata, A.; Fujita, T.; Chen, M. Nanoporous metal/oxide hybrid electrodes for electrochemical supercapacitors. *Nat. Nanotechnol.* **2011**, *6* (4), 232–236.
- (15) Brousse, T.; Bélanger, D.; Long, J. W. To be or not to be pseudocapacitive? *J. Electrochem. Soc.* **2015**, *162* (5), A5185–A5189.
- (16) Augustyn, V.; Come, J.; Lowe, M. A.; Kim, J. W.; Taberna, P. L.; Tolbert, S. H.; Abruña, H. D.; Simon, P.; Dunn, B. High-rate electrochemical energy storage through Li⁺ intercalation pseudocapacitance. *Nat. Mater.* **2013**, *12* (6), 518–522.
- (17) Hwang, J. Y.; El-Kady, M. F.; Wang, Y.; Wang, L.; Shao, Y.; Marsh, K.; Ko, J. M.; Kaner, R. B. Direct preparation and processing of graphene/RuO₂ nanocomposite electrodes for high-performance capacitive energy storage. *Nano Energy* **2015**, *18*, 57–70.
- (18) Santhanagopalan, S.; Balram, A.; Meng, D. D. Scalable high-power redox capacitors with aligned nanoforests of crystalline MnO₂ nanorods by high voltage electrophoretic deposition. *ACS Nano* **2013**, *7* (3), 2114–2125.
- (19) Come, J.; Augustyn, V.; Kim, J. W.; Rozier, P.; Taberna, P. L.; Gogotsi, P.; Long, J. W.; Dunn, B.; Simon, P. Electrochemical kinetics of nanostructured Nb₂O₅ electrodes. *J. Electrochem. Soc.* **2014**, *161* (5), A718–A725.
- (20) Kong, L.; Cao, X.; Wang, J.; Qiao, W.; Ling, L.; Long, D. Revisiting Li⁺ intercalation into various crystalline phases of Nb₂O₅ anchored on graphene sheets as pseudocapacitive electrodes. *J. Power Sources* **2016**, *309*, 42–49.
- (21) Le Viet, A.; Reddy, M. V.; Jose, R.; Chowdari, B. V. R.; Ramakrishna, S. Nanostructured Nb₂O₅ polymorphs by electrospinning for rechargeable lithium batteries. *J. Phys. Chem. C* **2010**, *114*, 664–671.
- (22) Griffith, K. J.; Forse, A. C.; Griffin, J. M.; Grey, C. P. High-Rate Intercalation without Nanostructuring in Metastable Nb₂O₅ Bronze Phases. *J. Am. Chem. Soc.* **2016**, *138* (28), 8888–8899.
- (23) Wang, X.; Li, G.; Chen, Z.; Augustyn, V.; Ma, X.; Wang, G.; Dunn, B.; Lu, Y. High Performance Supercapacitors Based on Nanocomposites of Nb₂O₅ Nanocrystals and Carbon Nanotubes. *Adv. Energy Mater.* **2011**, *1*, 1089–1093.
- (24) Kong, L.; Zhang, C.; Wang, J.; Qiao, W.; Ling, L.; Long, D. Free-standing T-Nb₂O₅/graphene composite papers with ultrahigh gravimetric/volumetric capacitance for Li-ion intercalation pseudocapacitor. *ACS Nano* **2015**, *9* (11), 11200–11208.
- (25) Lim, E.; Kim, H.; Jo, C.; Chun, J.; Ku, K.; Kim, S.; Lee, H. I.; Nam, I. S.; Yoon, S.; Kang, K.; Lee, J. Advanced hybrid supercapacitor based on a mesoporous niobium pentoxide/carbon as high-performance anode. *ACS Nano* **2014**, *8* (9), 8968–8978.
- (26) Kong, L.; Zhang, C.; Zhang, S.; Wang, J.; Cai, R.; Lv, C.; Qiao, W.; Ling, L.; Long, D. High-power and high-energy asymmetric supercapacitors based on Li⁺-intercalation into a T-Nb₂O₅/graphene pseudocapacitive electrode. *J. Mater. Chem. A* **2014**, *2* (42), 17962–17970.
- (27) Song, M. Y.; Kim, N. R.; Yoon, H. J.; Cho, S. Y.; Jin, H. J.; Yun, Y. S. Long-lasting Nb₂O₅-based nanocomposite materials for Li-ion storage. *ACS Appl. Mater. Interfaces* **2016**, *9*, 2267.
- (28) Lim, E.; Jo, C.; Kim, H.; Kim, M. H.; Mun, Y.; Chun, J.; Ye, Y.; Hwang, J.; Ha, K. S.; Roh, K. C.; Kang, K. Facile Synthesis of Nb₂O₅@Carbon Core–Shell Nanocrystals with Controlled Crystalline Structure for High-Power Anodes in Hybrid Supercapacitors. *ACS Nano* **2015**, *9* (7), 7497–7505.
- (29) Zhang, C. J.; Beidaghi, M.; Naguib, M.; Lukatskaya, M. R.; Zhao, M. Q.; Dyatkin, B.; Cook, K. M.; Kim, S. J.; Eng, B.; Xiao, X.; Long, D. Synthesis and charge storage properties of hierarchical niobium pentoxide/carbon/niobium carbide (MXene) hybrid materials. *Chem. Mater.* **2016**, *28* (11), 3937–3943.
- (30) Zhang, C. J.; Kim, S. J.; Ghidui, M.; Zhao, M. Q.; Barsoum, M. W.; Nicolosi, V.; Gogotsi, Y. Layered Orthorhombic Nb₂O₅@Nb₄C₃T_x and TiO₂@Ti₃C₂T_x Hierarchical Composites for High Performance Li-ion Batteries. *Adv. Funct. Mater.* **2016**, *26* (23), 4143–4151.
- (31) Xu, Y.; Lin, Z.; Zhong, X.; Huang, X.; Weiss, N. O.; Huang, Y.; Duan, X. Holey graphene frameworks for highly efficient capacitive energy storage. *Nat. Commun.* **2014**, *5*, 4554.
- (32) Girard, H. L.; Dunn, B.; Pilon, L. Simulations and interpretation of three-electrode cyclic voltammograms of pseudocapacitive electrodes. *Electrochim. Acta* **2016**, *211*, 420–429.
- (33) Wang, H.; Thiele, A.; Pilon, L. Simulations of cyclic voltammetry for electric double layers in asymmetric electrolytes: a generalized modified Poisson–Nernst–Planck model. *J. Phys. Chem. C* **2013**, *117* (36), 18286–18297.
- (34) Pilon, L.; Wang, H.; d’Entremont, A. Recent advances in continuum modeling of interfacial and transport phenomena in electric double layer capacitors. *J. Electrochem. Soc.* **2015**, *162* (5), A5158–A5178.
- (35) Girard, H. L.; Wang, H.; d’Entremont, A.; Pilon, L. Physical interpretation of cyclic voltammetry for hybrid pseudocapacitors. *J. Phys. Chem. C* **2015**, *119* (21), 11349–11361.
- (36) Girard, H. L.; Wang, H.; d’Entremont, A. L.; Pilon, L. Enhancing faradaic charge storage contribution in hybrid pseudocapacitors. *Electrochim. Acta* **2015**, *182*, 639–651.
- (37) Lindström, H.; Södergren, S.; Solbrand, A.; Rensmo, H.; Hjelm, J.; Hagfeldt, A.; Lindquist, S. E. Li⁺ ion insertion in TiO₂ (anatase). 2. Voltammetry on nanoporous films. *J. Phys. Chem. B* **1997**, *101* (39), 7717–7722.
- (38) Zhang, C. J.; Maloney, R.; Lukatskaya, M. R.; Beidaghi, M.; Dyatkin, B.; Perre, E.; Long, D.; Qiao, W.; Dunn, B.; Gogotsi, Y. Synthesis and electrochemical properties of niobium pentoxide deposited on layered carbide-derived carbon. *J. Power Sources* **2015**, *274*, 121–129.
- (39) Marcano, D. C.; Kosynkin, D. V.; Berlin, J. M.; Sinitskii, A.; Sun, Z.; Slesarev, A.; Alemany, L. B.; Lu, W.; Tour, J. M. Improved synthesis of graphene oxide. *ACS Nano* **2010**, *4* (8), 4806–4814.
- (40) Cullity, B. D.; Stock, S. R. *Elements of X-ray Diffraction*, 3rd ed.; Prentice-Hall: Upper Saddle River, NJ, 2001.
- (41) Levi, M. D.; Lukatskaya, M. R.; Sigalov, S.; Beidaghi, M.; Shpigel, N.; Daikhin, L.; Aurbach, D.; Barsoum, M. W.; Gogotsi, Y. Solving the capacitive paradox of 2D MXene using electrochemical quartz-crystal admittance and in situ electronic conductance measurements. *Adv. Energy Mater.* **2015**, *5* (1), 1400815.
- (42) Pérez, C. R.; Yeon, S. H.; Ségalini, J.; Presser, V.; Taberna, P. L.; Simon, P.; Gogotsi, Y. Structure and electrochemical performance of carbide-derived carbon nanopowders. *Adv. Funct. Mater.* **2013**, *23* (8), 1081–1089.